Effects of angle of attack on the large oscillations of a thin elliptical cylinder

Jonathan C.C. Lo [a],[*], Mark C. Thompson [a], Kerry Hourigan [a], Jisheng Zhao [a],[b]

[a] *Fluids Laboratory for Aeronautical and Industrial Research (FLAIR), Department of Mechanical and Aerospace Engineering, Monash University, Victoria 3800, Australia*
[b] *School of Engineering and Technology, University of New South Wales, Canberra, ACT 2600, Australia*

ARTICLE INFO

ABSTRACT

The effect of angle of attack on the flow-induced vibration (FIV) response of an elastically mounted thin elliptical cylinder has been investigated by measuring the structural displacement and fluid forces acting on the body in water-channel experiments. Specifically, an elliptical cylinder with a cross-sectional elliptical ratio of $\varepsilon = b/a = 5$ was chosen due to the presence of a region of vibration response associated with the combined effect of vortex-induced vibration (VIV) and galloping, where large vibration amplitudes nearly eight times the cross-flow dimensions can be sustained. Here, a and b are the semi-minor axis (aligned with the streamwise direction) and the semi-major axis, respectively. The present experimental results demonstrated that the large vibration amplitudes (i.e. where the maximum observed value was approximately $6b$) generally decrease with the angle of attack, resulting in substantial reductions for $\alpha \gtrsim 2°$ (with $\alpha = 3.50°$ corresponding to a $\sim 60\%$ decrease in the maximum vibration amplitude). Particle image velocimetry (PIV) measurements revealed that the dominant vortex shedding mode consists of two single opposite-signed vortices shed per body vibration cycle. The presence of additional vorticity regions that were absent in the zero angle of attack case was also observed, including crescent-shaped wake structures and secondary inline vortices. This study shows the importance of maintaining axial symmetry in such an FIV system, and that the flow incidence angle is an essential consideration for efficient energy harvesting using this elliptical geometry.

1. Introduction

Flow-induced vibration (FIV), arising from the coupled interaction between a fluid and a structure (often termed fluid–structure interaction), is an important phenomenon prevalent in many engineering applications. Traditionally, FIV is considered a detrimental phenomenon in applications such as bridges and high-rise buildings where structural failure and long-term fatigue are undesirable. However, since the pioneering study of Bernitsas et al. (2008), there has also been significant research interest in harnessing the kinetic energy from FIV as a potential source of renewable energy (Lv et al., 2021; Soti et al., 2018; Wang et al., 2017). As such, this has motivated ongoing investigations to characterise, to predict, and to control FIV, with the rich body of literature arising from this research progress comprehensively summarised in previous literature reviews (e.g. Blevins, 1990; Naudascher and Rockwell, 2017; Païdoussis et al., 2010).

Nomenclature

**Symbols**

a	Streamwise diameter of elliptical cylinder
b	Cross-flow diameter of elliptical cylinder
c	Damping coefficient
C_v	Vortex force coefficient
C_x	Drag force coefficient
C_y	Lift force coefficient
f_{na}	Natural frequency in quiescent air
f_{nw}	Natural frequency in quiescent water
F_v	Vortex force
F_x	Drag force
F_y	Lift force
k	Spring constant
L	Immersed length of cylinder
m	Mass of oscillating system
m^*	Mass ratio
m_A	Added mass
Re	Reynolds number
St	Strouhal number
U	Freestream velocity
U^*	Reduced velocity
y	Body displacement
$\dot{y}$	Body velocity
$\ddot{y}$	Body acceleration
y^*	Normalised body displacement
α	Angle of attack of the elliptical cylinder relative to the freestream
ε	Elliptical ratio of cylinder
ζ	Damping ratio
ν	Kinematic viscosity of water
ρ	Density of water

Depending on excitation sources, FIV of structures is typically characterised by two distinct phenomena: vortex-induced vibration (VIV) and galloping. VIV is caused by the periodic or quasi-periodic shedding of vortices behind a bluff body, typically with the body vibration amplitude self-limited to the order of one body diameter. Galloping, on the other hand, is driven by unsteady movement-induced aerodynamic forces and is typically characterised by a body vibration amplitude response linearly increasing with reduced flow velocity but with the dominant vibration frequency much lower than that of the natural vortex shedding. Whilst many works have investigated both VIV and galloping individually through the use of circular and square geometries, respectively, recent studies (Nemes et al., 2012; Zhao et al., 2014b, 2018a) have shown that rich, complex, and nonlinear fluid–structure interactions can also be observed when both of these FIV phenomena occur jointly in the dynamic response of an elastically mounted cylinder.

One example of the coupling between VIV and galloping may occur when the cross-sectional profile of a circular cylinder is deformed to an elliptical cylinder. The resultant elliptical cross-section is characterised by the elliptical ratio $\varepsilon = b/a$, where a and b are the streamwise and cross-flow dimensions, respectively. Zhao et al. (2019) studied the effect of elliptical ratio over the range $0.67 \leqslant \varepsilon \leqslant 1.50$ on the FIV response for a mass ratio of $m^* = 6.00$ at moderate Reynolds numbers ($860 \leqslant \text{Re} \leqslant 8050$). They discovered that, as ε was increased, wake-body synchronisation tended to occur at lower reduced velocities than for the circular case. Furthermore, peak vibration amplitude was observed to increase with the elliptical ratio, concurring with the earlier results of Navrose et al. (2014) for a mass ratio of $m^* = 10.0$, and a Reynolds number and elliptical ratio range of $60 \leqslant \text{Re} \leqslant 140$ and $0.7 \leqslant \varepsilon \leqslant 1.43$, respectively.

Interestingly, in the extreme case of a transversely oscillating thin elliptical cylinder with an elliptical ratio of $\varepsilon = 5$, Lo et al. (2023) showed that vibrations nearly eight times the cross-flow dimension can be sustained with a main frequency that matches the natural frequency of the system in quiescent water. Such substantial amplitudes occur in a region that is associated with the combined effect of VIV and galloping. Furthermore, as large oscillations were present even with a degree of structural damping, a potential application includes using the FIV response of thin elliptical cylinders as a means of power extraction from a flow.
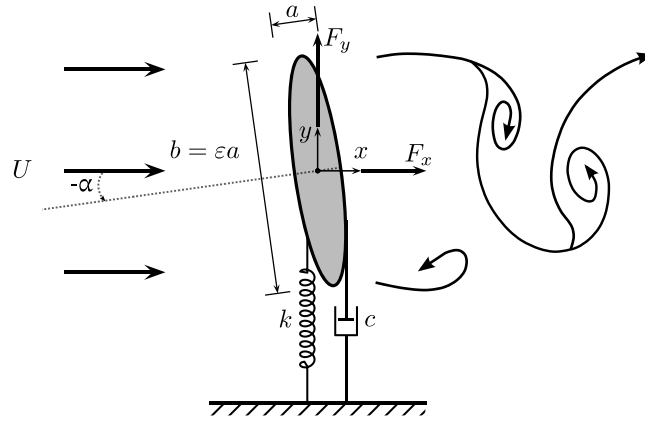
Fig. 1. A schematic defining the problem of interest: an elastically mounted elliptical cylinder model constrained to oscillate transverse (y) to the velocity U of the freestream, which is in the positive x direction. Additionally, m is the oscillating mass, k is the spring constant, c is the structural damping, α is the angle of attack of the body relative to the freestream, and F_x and F_y represent the respective drag and the transverse (lift) fluid forces acting on the body.

Given the dramatic increase in FIV of a thin elliptical cylinder over a circular cylinder, understanding the effect of angle of attack (i.e. to further break the symmetry of the fluid–structure system) on the FIV dynamics of a thin elliptical cylinder is needed. As the underlying symmetry of a system can restrict the types of flow states that can occur, we expect that the introduction of a non-zero orientation angle will lead to wake structures that cannot be achieved in symmetric cases. Examples in the literature of symmetry breaking by varying the angle of attack include Nemes et al. (2012) and Zhao et al. (2014c) for square cylinders, and Massai et al. (2018) for a low-side-ratio rectangular cylinder. For the square cylinder in Nemes et al. (2012), it was found that at angles of attack over the range $10 \leqslant \alpha \leqslant 22.5°$, the symmetry breaking results in a sub-harmonic vibration mode (coined the "higher branch"), where the cylinder vibration amplitudes were larger than those in the upper branch. In the case of elliptical cylinders, Leontini et al. (2018) numerically investigated an ellipse with a mild aspect ratio (major to minor axis length) of $\Gamma = 1.5$ that is close to 1 (i.e. geometrically similar to a circular cylinder) and found marked differences in the behaviour of the cylinder depending on its orientation angle. At $\theta = 0°$, where the semi-major axis is aligned parallel to the oncoming flow, the FIV response was similar to that of a circular cylinder. This resemblance was suppressed at greater angles (i.e. $40° < \theta \leqslant 90°$), and the FIV response was characterised by "large-amplitude" oscillations (i.e. maximum amplitudes approximately two times larger than in the $\theta = 0°$ case) that occurred over the entire range of reduced velocity. However, to the authors' knowledge, the effect of the angle of attack on elastically mounted thin elliptical cylinders has not been investigated.

To summarise, the literature has shown that the extreme eccentricity of the $\varepsilon = 5$ elliptical cylinder gives rise to interesting FIV dynamics resulting from the joint occurrence of both VIV and galloping. However, the impact of further symmetry breaking, in the form of a non-zero orientation angle between the cylinder and the oncoming flow, on the FIV response remains unclear. Elucidating this effect could have wide-ranging implications, especially in the field of renewable energy generation where there has been significant research interest in using the FIV of bluff bodies to extract power from the moving fluid (Bernitsas et al., 2008; Ding et al., 2016; Lv et al., 2021). Whilst the large oscillations achieved by Lo et al. (2023) were observed when the flow is exactly normal to the semi-major axis of the cylinder, the incidence angle of naturally occurring flows may vary over time. However, as far as the authors are aware, no study to date has addressed the impact of orientation angle on the FIV of thin elliptical cylinders for flow conditions and structural parameters conducive to high vibration amplitudes. Therefore, filling this gap in the literature will provide greater insights into factors that may affect the energy generation performance of methods based on elliptical geometries.

This study presents an experimental investigation into the influence of the angle of attack on the FIV response of a thin elliptical cylinder with an elliptical ratio of $\varepsilon = 5$. The FIV response is characterised as a function of reduced velocity over a range of selected angles of attack $\alpha = [0.00°, 1.75°, 2.00°, 2.50°, 3.50°]$. In particular, the dynamics of the FIV system will be examined based on an overall evaluation of the amplitude and frequency responses, as well as the fluid forces and their phases relative to the body displacement. The observed wake modes will also be presented to provide a further understanding of the complex fluid–structure interaction that causes these oscillations.

2. Experimental method

The dynamic response of the thin elliptical cylinder (Fig. 1) was investigated by modelling the transverse FIV system as a second-order mass–spring–damper oscillator subjected to a free-stream flow, with the body displacement $y(t)$ due to the transverse fluid force $F_y(t)$ governed by

$$m\ddot{y}(t) + c\dot{y}(t) + ky(t) = F_y(t), \tag{1}$$

where m is the total oscillating mass, and c and k are the structural damping and spring constants, respectively. The modelling of the fluid–structure system was conducted experimentally in the recirculating water channel facilities of the *FLAIR group* at Monash
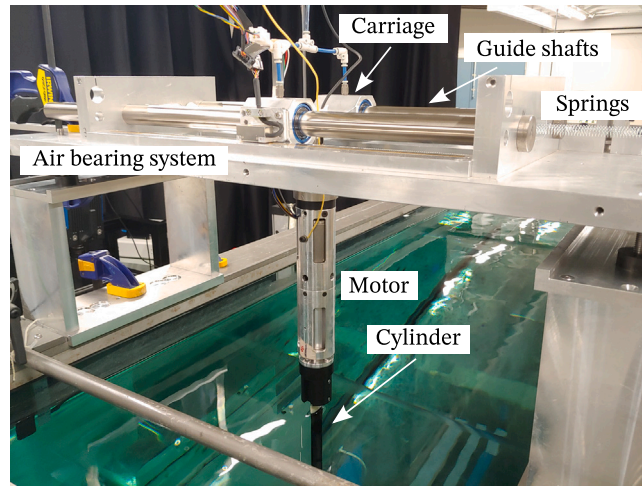
Fig. 2. A labelled photograph detailing the experimental set-up, consisting of a cylinder connected to the motor, which in turn is mounted to the air bearing system situated on top of the water channel.

University, where the freestream turbulence level in the test section was less than 1%. The test section has dimensions of 600 mm in width, 800 mm in depth and 4000 mm in length, with further details of the water channel facility provided in Zhao et al. (2014c) and Sherry et al. (2010).

The setting of the angle of attack (α) was implemented through a brushless servo motor (model EC-i40, Maxon Group) equipped with an optical rotary encoder (model ENC 16 RIO with 4096 counts per turn, Maxon Group) that had an angular resolution of 0.02°, and electronically controlled using Beckhoff TwinCAT® 3 software with a motor controller (model MAXPOS 50/5, Maxon Group) acting as the hardware interface. Both the cylinder and motor were then elastically mounted on a low-friction air-bearing system that had been tested and validated (Zhao et al., 2018a,b), thus constraining the motion to only be in the cross-flow direction. The transverse displacement was measured using a digital linear encoder with a resolution of 1 μm (model RGH24; Renishaw, UK), which was then differentiated to obtain the velocity and acceleration needed to calculate the transverse lift force. However, the streamwise drag forces were instead obtained using a force sensor (model Mini40, ATI-IA, USA). Data acquisition at a sampling rate of 100 Hz was also undertaken using the TwinCAT software, with the hardware interface provided by Beckhoff Automation GmbH EtherCAT digital I/O modules. A diagram of the full experimental set-up is presented in Fig. 2.

The elliptical cylinder model tested had an elliptical ratio of $\varepsilon = b/a = 5$, where $b = 25 \pm 0.10$ mm and $a = 5 \pm 0.10$ mm were the cross-flow and stream-wise dimensions, respectively. The immersed length of the cylinder was $L = 450 \pm 0.5$ mm, giving a length-to-diameter (aspect) ratio of $L/b = 18.0$. The resulting mass ratio was $m^* = m/m_d = 53$, with $m = 2337.1 \pm 0.05$ g and $m_d = \rho\pi abL/4$ being the total oscillating mass and displaced mass of fluid of density ρ, respectively. The applied structural damping was described by the damping ratio, $\zeta = c/(2\sqrt{k(m + m_A)}) = 1.5 \times 10^{-3}$, where m_A is the added mass (in potential flow). To promote parallel vortex shedding by suppressing end effects, an end-conditioning platform was positioned approximately 1 mm (4% of b) below the free end of the cylinder (see Khalak and Williamson (1996)). The use of the platform to reduce end effects has been validated and utilised extensively by Zhao et al. (2014b, 2018b), Wong et al. (2017), and Soti et al. (2018).

The body vibration was characterised by the normalised amplitude $A^* = A/b$ and reported as A^*_{10}, the mean of the top 10% of peak amplitudes. The FIV dynamics were evaluated as a function of reduced velocity, $U^* = U/(f_{nw}b)$, with f_{nw} being the natural frequency of the system in quiescent water. To determine both the natural frequency of the system and structural damping ratios, free-decay tests were conducted individually in both quiescent air and water, resulting in $f_{na} = 0.717 \pm 0.001$ Hz and $f_{nw} = 0.716 \pm 0.001$ Hz, respectively.

The reduced velocity range of interest was $3 \leqslant U^* \leqslant 10$, corresponding to a freestream velocity range of $52 \leqslant U \leqslant 179$ mm s^{-1} and a Reynolds number range of $1250 \leqslant \text{Re} = UD/\nu \leqslant 4450$, with ν being the kinematic viscosity of the water. Due to the operational range of the force sensor used to measure the drag acting on the elliptical cylinder, a limit of $A = 150$ mm, which is approximately equal to $A^* \approx 6$, was imposed on the experiments. This limit was only reached for the $\alpha = 0°$ curve when $U^* \approx 7$, and as such, the structural dynamics beyond this reduced flow could not be measured.

It should also be noted that in the present study, streamwise drag and the transverse lift are described in dimensionless forms defined by $C_x = F_x/(\rho U^2 bL/2)$ and $C_y = F_y/(\rho U^2 bL/2)$, respectively. In addition, the dimensionless form of the vortex force is given by $C_v = F_v/(\rho U^2 bL/2)$, which can be computed through a decomposition of the total transverse force into a vortex force component (F_v) and a potential force component (F_P), namely $F_y = F_v + F_P$, with the potential force in an inviscid fluid being $F_P = -m_A\ddot{y}$ (Govardhan and Williamson, 2000; Morse and Williamson, 2009; Zhao et al., 2014a,b).

To observe the wake structures associated with the body oscillations, Particle Image Velocimetry (PIV) was employed to visualise a cross-sectional plane in the near wake of the cylinder. The flow was seeded using hollow micro-spheres (model Sphericel 110P8; Potters Industries Inc.) of normal diameter 13 μm and specific weight 1.10 g cm^{-3}, with illumination provided by a 3 mm thick laser

sheet from a 5 W continuous laser (model: MLL-N−532 nm-5 W, CNI). The images were then captured using a high-speed camera (Dimax S4, PCO AG, Germany) equipped with a 50 mm lens (Nikon Corporation, Japan), resulting in a resolution of 2016×2016 pixel^2 and an optical magnification factor of approximately 6.23 pixel mm^{-1}. For each trial, a set of 3100 image pairs was recorded at a sampling rate of 10 Hz. Validated in-house software, originally developed by Fouras et al. (2008), was then used to correlate 32×32 pixel^2 interrogation windows with 50% window overlap to obtain the time-dependent vector fields of the wake flow. Finally, employing a phase-band technique, the resultant fields were averaged using a phase portrait with the cylinder displacement and velocity as the x and y axis, respectively. Since PIV measurements were sampled at random points of the body motion, transistor–transistor logic (TTL) pulses were first used to synchronise the PIV measurements with the digital linear encoder signal to determine the cylinder's displacement and velocity for each vector field. From this information, the fields were then sorted into 48 different regions based on their location in the phase portrait, with averaging conducted over each bin. As such, each region corresponds to a specific time interval within the body oscillation period (for more details, see Zhao et al. (2014c)).

2.1. Results and discussion

To fully elucidate and characterise the effect of angle of attack on the dynamics of the $\varepsilon = 5$ elliptical cylinder, an overall evaluation of the amplitude and frequency responses, as well as the fluid forces and their mean phase relative to the body displacement, was conducted. Fig. 3($a.i$) shows the normalised amplitude response as a function of reduced velocity (with increasing U^* increments) for the five angles of attack (α) of interest. The transverse fluid force (C_y), vortex force (C_v), and streamwise drag force (C_x) are additionally presented in Figs. 3($a.ii$), 5($a.i$), and 5($a.ii$), respectively. The corresponding normalised power spectral density (PSD) frequency contours of the body vibration (f_y^*) and transverse force ($f_{C_y}^*$), as well as the vortex force ($f_{C_v}^*$), and drag force ($f_{C_x}^*$), are shown for each angle in Fig. 3(b–f) and Fig. 5(b–f), respectively. Here, the frequency components are normalised by f_{nw}; e.g. $f_y^* = f_y/f_{\mathrm{nw}}$.

2.1.1. Impact of the angle of attack on the overall dynamic response

Before discussing the angle-of-attack effect on the FIV dynamics of the elliptical cylinder, the case at zero angle of attack ($\alpha = 0°$) for increasing U^* increments will be discussed and used as a baseline to highlight how the resultant dynamics changes with increasing α values.

As shown in Fig. 3(b), the FIV response at $\alpha = 0°$ can be separated into two different wake-body synchronisation regimes: Regime I and Regime II, which is in line with the naming convention proposed by Lo et al. (2023). Here, wake body synchronisation is represented by the matching of the dominant frequencies of f_y^* and $f_{C_y}^*$, which occurs at f_{nw}. Regime I corresponds to an amplitude response A_{10}^* exhibiting an almost linear growth with increasing U^* and a negligible mean phase difference ($\phi_y \approx 10°$, see Fig. 4) between the body motion and the transverse fluid force. Although the fluid forcing frequency also sees a weak second harmonic component (i.e. $f_{C_y}^* \simeq 2$), the dynamics of Regime I resemble that of the initial branch of a circular cylinder. However, as the reduced velocity is increased beyond $U^* \approx 4$, the onset of Regime II is marked by the emergence of a third harmonic in $f_{C_y}^*$, with the strength of both the second and third harmonics increasing with reduced velocity until the limits of the experimental rig were reached at $U^* \approx 7$.

From Fig. 3($a.i$), the loss of axial symmetry through varying α leads to reductions in the body vibration amplitude over the entire reduced velocity range of interest. Whilst wake-body synchronisation is present over approximately the same reduced velocity range for $\alpha \geqslant 1.75$, the U^* range over which the different synchronisation regimes occur varies significantly with α.

Although the FIV response curve does not change significantly as α is increased from $\alpha = 0°$ to $1.75°$, the amplitude reduction is sufficient to allow the FIV response over the entire U^* range to be captured without exceeding the limits of the experimental set-up. As such, a new wake-body synchronisation regime is observed, which has not been seen previously for the symmetric baseline case (i.e. $\alpha = 0°$, see Fig. 3(b)). Due to the asymmetric nature of this newly classified regime, we will henceforth refer to this region as "A1". From the representative case in Fig. 6(a), regime A1 also sees contributions from a galloping-like movement-induced instability and is characterised by the second harmonic in the fluid forcing ($f_{C_y}^* \simeq 2$) overtaking $f_{C_y}^* \simeq 1$ as the dominant frequency. Additionally, for $U^* > 7$, a desynchronisation region appears, where the frequency response of the transverse lift becomes broad band and centred on the Strouhal vortex shedding frequency of the fixed body f_{St} (Fig. 3($c.ii$)). The same contribution is also observed in the body vibration PSD contours, in addition to a broadband spectra close to the natural frequency of the system in water. Note that the Strouhal number was experimentally measured to be $\mathrm{St} = f_{\mathrm{St}} b/U = 0.169$ for the fixed cylinder case.

Interestingly, only a small angle of just $\alpha = 2.00°$ is required to significantly attenuate the large vibrations associated with Regime II. This α case sees the appearance of another VIV-dominated regime, which is characterised by a monotonically decreasing A_{10}^* trend with increasing U^*. The onset of this region corresponds to three distinct behaviours. First, a step-like increase in the body and transverse fluid force frequencies to $1.06f_{\mathrm{nw}}$ occurs. Unlike the frequency response in Regime II, the contributions of the harmonic frequency components in this second VIV-dominated regime gradually increase with U^*. Second, the contribution of the second and third harmonics of the fluid-force frequency response ($f_{C_y}^*$) becomes negligible, with the first harmonic being the dominant frequency component. Third, a phase jump to a plateau of $\phi_y \simeq 180°$ is observed at the onset of this regime, thereby indicating that the relationship between body motion and total transverse force is predominantly anti-phase in nature. As such, in line with the FIV response characterisation of Lo et al. (2023) for an $\varepsilon = 5$ elliptical cylinder under applied structural damping, this VIV-dominated regime is henceforth referred to as Regime III. Additionally, it is also observed that the vibration amplitude and the reduced velocity range of this regime are independent of the angle of attack for $\alpha \geqslant 2.00°$.
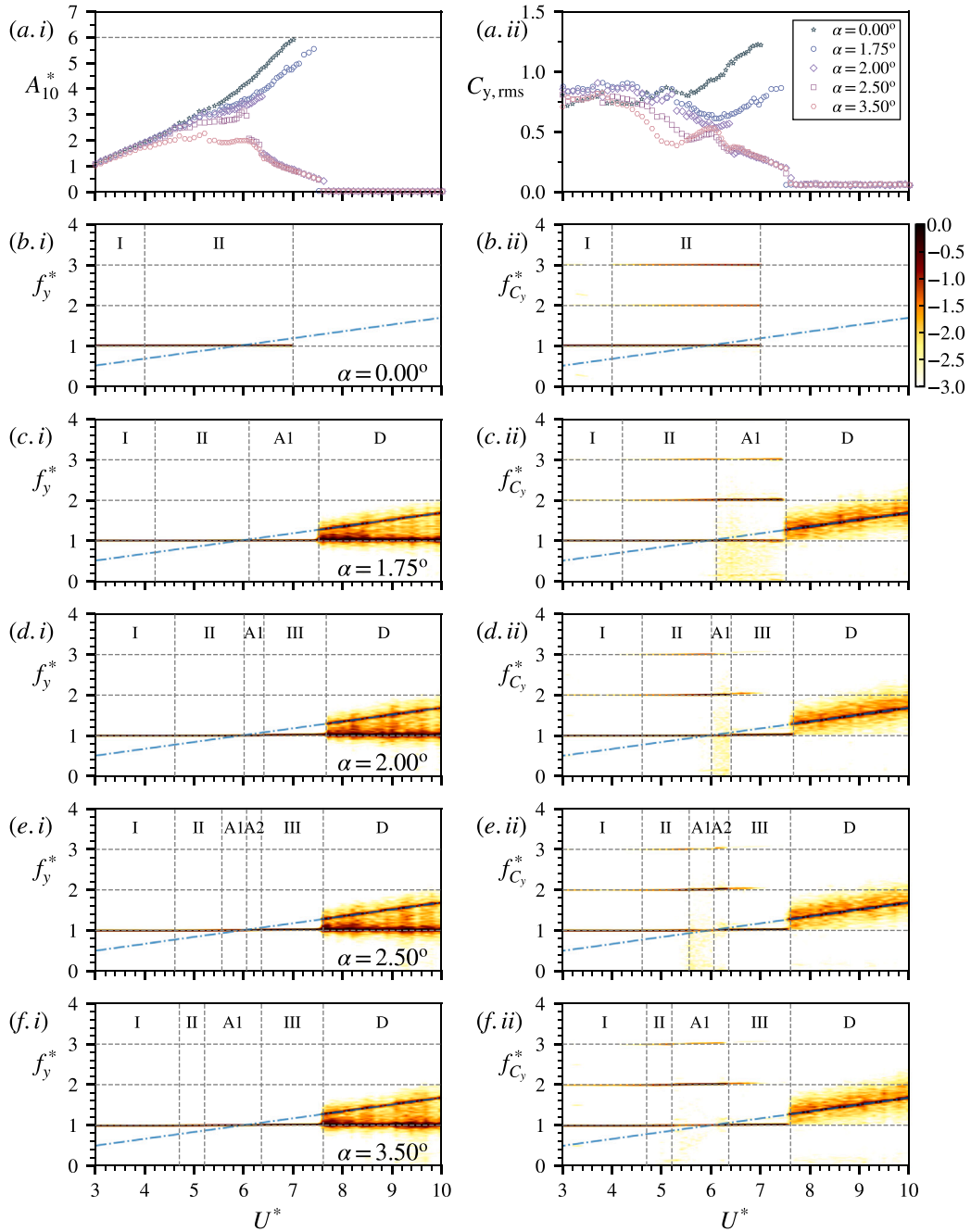
Fig. 3. (a.i) The normalised amplitude response (increasing U^*) and (a.ii) root-mean-square of the transverse force coefficient as a function of U^* for all α values of interest. ((b–f).i) The logarithmic-scale power spectral density (PSD) contours of the corresponding normalised vibration (f_y^*), and ((b–f).ii) the transverse fluid force ($f_{C_y}^*$) frequencies are also presented for each angle of attack. In (b)–(f), the horizontal dashed line highlights the frequencies at $f^* \in \{1, 2, 3\}$; the vertical dashed lines represent the boundaries of different response regimes (i.e. Regime I, II, III, first asymmetric region (A1), second asymmetric region (A2) and desynchronisation (D)); the horizontal dashed line at $A^* = 6$ in (a.i) represents the imposed vibration limit due to the physical limitations of the present experimental set-up; and the sloped blue dot-dashed line represents the Strouhal number (St $= f_{St}b/U = 0.169$, where f_{St} is the Strouhal vortex shedding frequency) measured for a stationary cylinder. (For interpretation of the references to colour in this figure legend, the reader is referred to the web version of this article.)

Another asymmetric regime (labelled "A2") of wake-body synchronisation that is also partially driven by movement-induced galloping occurs at $\alpha = 2.50°$. As can be seen in Fig. 3(a.i), this regime corresponds to an intermediate vibration amplitude branch that separates from the branch of monotonically increasing amplitudes with U^* (i.e. consisting of Regime I, II, and A1), and Regime
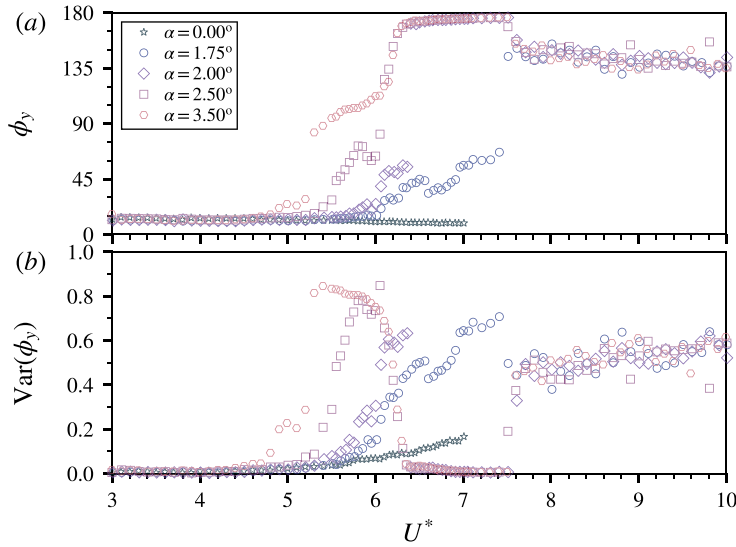
Fig. 4. (a) The time-mean phase ϕ_y between the body motion ($y^* = y/b$) and the total transverse fluid force (C_y) and (b) the corresponding variance value Var(ϕ_t) are shown as a function of reduced velocity (U^*) over a range of angles of attack (α).

III. Similar to Regime III, the onset of Regime A2 is marked by a step-like increase in the body vibration and transverse fluid force frequencies. Furthermore, whilst $f_{C_y}^* \simeq 2$ is the dominant frequency in Regime A1, the second observed asymmetric region in Regime A2 is characterised by an almost equal contribution by $f_{C_y}^* \simeq 1$ and 2 to the frequency response and a weak contribution by $f_{C_y}^* \simeq 3$ as shown in Fig. 6(b).

Though the amplitude response retains multiple branches for $\alpha \leqslant 2.50°$, a collapse to a single branch is seen for a larger α case at 3.50°. Additionally, suppression of Regime A2 is observed, leaving Regime A1 as the sole asymmetric region present. Interestingly, the vibration amplitudes in Regime II and Regime A1 appear to be relatively independent of reduced velocity, with a mean amplitude of $A_{10}^* = 1.95$ observed.

2.1.2. Effect of angle of attack on fluid forcing and phase angles

An integral aspect of the fluid–structure interaction concerns the forces exerted by the flow on the elastically mounted elliptical cylinder, as well as their relative phases with respect to the body displacement. Fig. 3(a.ii) shows the root mean square (r.m.s.) values of the transverse fluid force coefficient as a function of reduced velocity. Whilst $C_{y_{rms}}$ increases slightly with α for $U^* \leqslant 4$, the transverse fluid forcing is significantly reduced by increasing α for Regime II and the asymmetric regimes (i.e. A1 and A2) when the reduced velocity is greater than $U^* \approx 5$. This striking reduction in the transverse fluid force coefficient at small α indicates that the movement-induced instability that drives the galloping-like component of the FIV dynamics is strongly affected by any breaking of the inherent symmetry in the system. However, an exception to the above trend exists for Regime A1 $\alpha \geqslant 2.50°$, where the local peak in C_y increases with α instead. This departure from the trend will be further discussed when analysing the vortex forces. For Regime III, the vibration amplitude and transverse fluid force are unaffected by the α values as considered here, implying that small violations of the symmetry do not affect the VIV-dominated dynamics of the thin elliptical cylinder.

In terms of the phase between the total transverse fluid force (ϕ_y) and the body motion, Fig. 4(a) shows the mean phase value for the various angles of attack tested. Due to the circular nature of this quantity, ϕ_t is calculated from the mean vector ($\bar{\mathbf{\Phi}}$) of the instantaneous phases ($\phi_{\text{total,j}}$) over the recording period consisting of N samples (McQueen et al., 2021; Zhao et al., 2022), expressed as

$$\bar{\mathbf{\Phi}} = \frac{1}{N} \sum_{j=1}^{n} e^{i\phi_{\text{total,j}}}, \tag{2}$$

$$\phi_y = \text{Arg}(\bar{\mathbf{\Phi}}), \tag{3}$$

$$\text{Var}(\phi_y) = 1 - |\bar{\mathbf{\Phi}}| \in [0, 1]. \tag{4}$$

Here, the variance value Var(ϕ_y) (Fig. 4(b)) is used as an indicator of phase synchronisation with a value of zero indicating that all phase angles are equal (i.e. perfect phase synchronisation), whereas a value of one indicates that phase angles are spread uniformly over the circular space (i.e. no phase synchronisation). As such, regimes I and III respectively correspond to an approximately in-phase and anti-phase relationship, as previously mentioned in Section 2.1.1. Additionally, the phase is also found to be strongly synchronised, as evidenced by the phase variance (Var(ϕ_y)) for both regimes remaining close to zero. However, due to the second harmonic being a dominant component in the y-direction forcing frequency response ($f_{C_y}^* \simeq 2$), the phase variance deviates
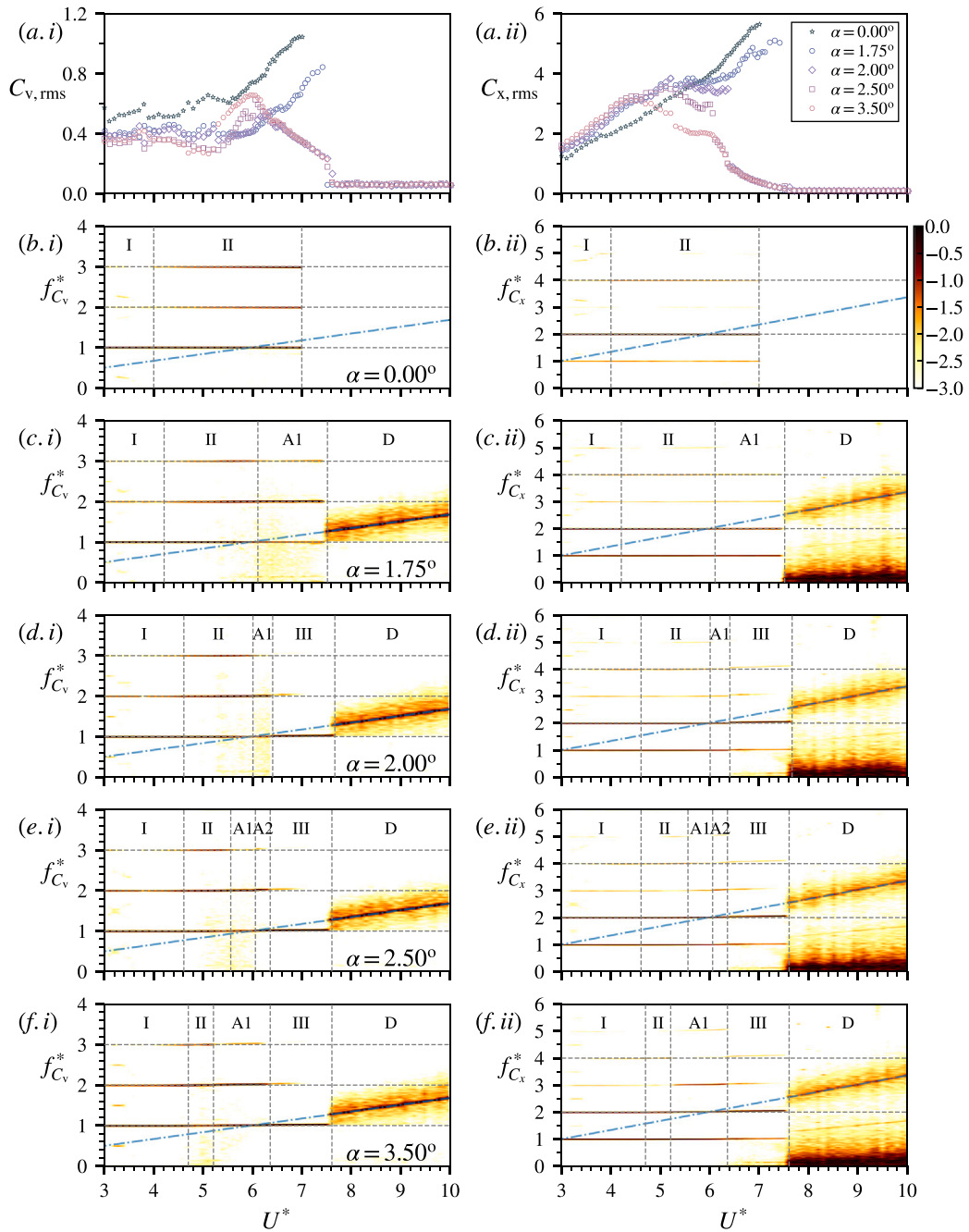
Fig. 5. ($a.i$) The root-mean-square of the vortex force and ($a.ii$) drag force coefficients (for increasing U^*) as a function of U^* for all α values of interest. ((b–f).i) The logarithmic-scale PSD contours of the corresponding vortex force ($f^*_{C_v}$), and ((b–f).ii) the streamwise drag force ($f^*_{C_x}$) frequencies are also presented for each angle of attack. In ((b–f).i) and ((b–f).ii), the horizontal dashed line highlights the frequencies at $f^* \in \{1,2,3\}$ and $f^* \in \{2,4,6\}$, respectively; the vertical dashed lines represent the boundaries of different response regimes; and the sloped blue dot-dashed line represents the Strouhal number (St = 0.169) and twice the Strouhal number measured for a stationary cylinder for ((b–f).i) and ((b–f).ii), respectively. (For interpretation of the references to colour in this figure legend, the reader is referred to the web version of this article.)

significantly from zero (Var(ϕ_y) > 0.2) for the asymmetric regimes (i.e. A1 and A2) as shown in Fig. 6. Thus, this indicates that the phase difference between the body motion and fluid forcing is not fully correlated, which further supports the conclusion that Regimes A1 and A2 are asymmetric in nature.

Fig. 5($a.i$) shows how the root-mean-square values of the vortex force coefficient ($C_{v\,rms}$) as a function of reduced velocity are affected by the angle of attack. Whilst $C_{v\,rms}$ generally decreases with increasing α, the opposite is true for Regime A1 when $\alpha \geqslant 2.50°$.
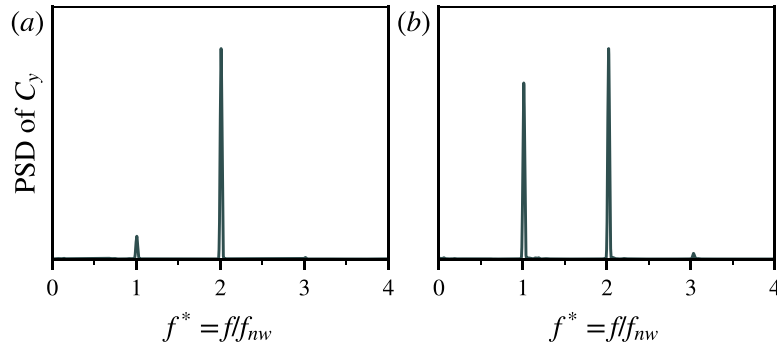
Fig. 6. Representative PSD taken from Fig. 3(*e.ii*) at $\alpha = 2.5°$ for (*a*) the first asymmetric regime where $U^* = 5.8$, and (*b*) the second asymmetric region where $U^* = 6.2$.
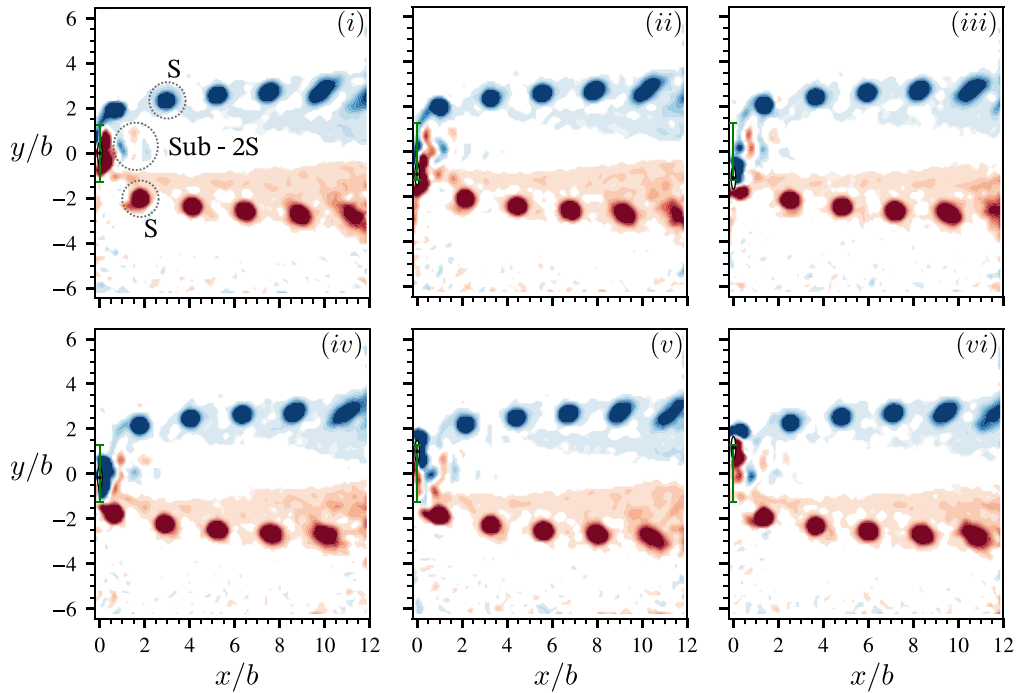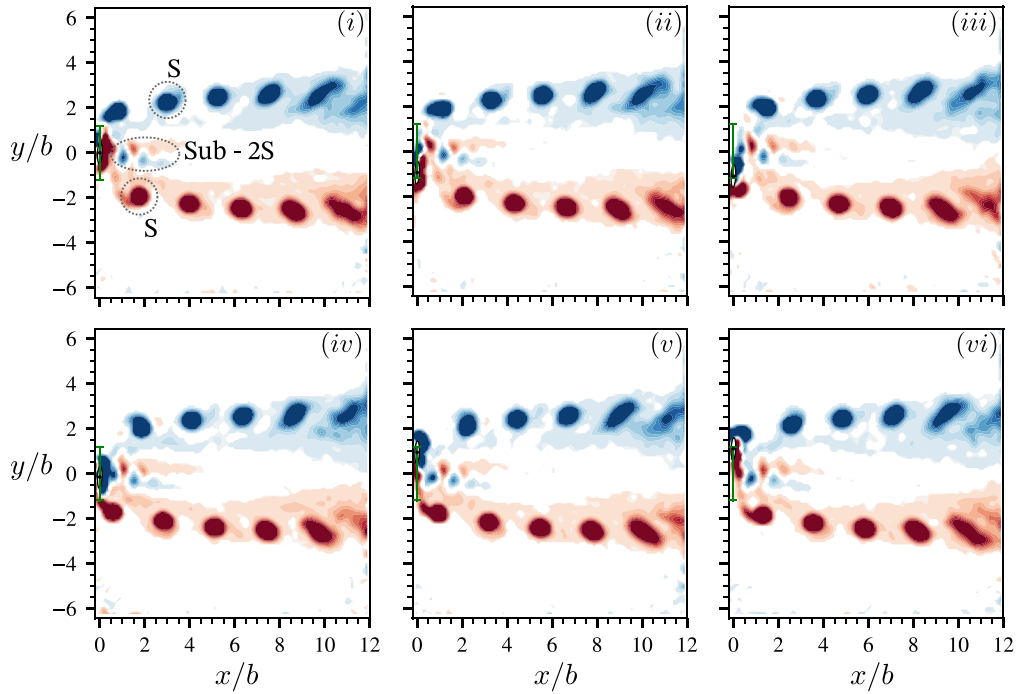

Fig. 7. Evolution of phase-averaged vorticity contours for angle of attack of $\alpha = 0°$ at $U^* = 3.2$ (Regime I), with the flow moving from left to right. The normalised vorticity field is $\omega_z^* = \omega_z b/U$, where ω_z is the vorticity out of the x-y plane. The blue and red contours represent clockwise and anti-clockwise vorticity, respectively. The black dot at the far left denotes the body centre position of the cylinder and the green vertical line between two horizontal bars indicates the peak-to-peak vibration amplitude. A single vortex is shed every half cycle as part of the observed 2S wake mode, with additional vorticity in the region between the counter-rotating vortex pair forming a secondary 2S wake mode (sub-2S). (For interpretation of the references to colour in this figure legend, the reader is referred to the web version of this article.)

Instead, the vortex force peaks around $U^* \approx 1/f_{St} = 5.92$, in contrast with the approximately monotonically increasing trend in Regime A1 that is observed for $\alpha \leqslant 2.50°$. As C_{vrms} provides an indication of the vortex dynamics that contribute to the FIV response, the peak in the impulse acting on the elliptical cylinder from the vorticity in the flow occurs when the vortex shedding frequency of a stationary cylinder matches the natural frequency of the system in quiescent water. This difference in the shape of the C_{vrms} curves for $\alpha \geqslant 2.50°$ implies that the movement-induced galloping has been significantly suppressed and suggests that the FIV response is predominantly driven by VIV instead. Like the transverse lift force coefficient, the vortex force coefficient for Regime III is also unaffected by the angle of attack, as evidenced by the general concurrence in C_{vrms} across all angles of attack for $\alpha \geqslant 2.00°$.

The frequency responses of the vortex force for each α case are also presented in Figs. 5((b–f).i). They are found to be very similar to their corresponding transverse lift frequency response Figs. 3((b–f).ii). However, the differences between the vortex force frequency response (Fig. 5($a.i$)) and the transverse lift frequency response (Fig. 3($a.ii$)) are associated with the differences in their relative phases with respect to the body motion.

Fig. 8. Evolution of phase-averaged vorticity contours for angle of attack of $\alpha = 2.5°$ at $U^* = 3.2$ (Regime I), with the flow moving from left to right. More details can be found in the caption of Fig. 7. The wake pattern is almost identical to that in Fig. 7, except with the secondary 2S wake mode (sub–2S) being stronger and more well-defined.

Finally, Fig. 5($a.ii$) shows the root-mean-square values of the drag force ($C_{x rms}$) as a function of reduced velocity for the angles of attack tested, along with the drag frequency response for each α case presented in Figs. 5(($b–f$).ii). The maximum streamwise drag force reduces in strength with increasing α due to the decrease in the maximum vibration amplitude arising from the wake pattern becoming more asymmetric. This is evidenced by the strengthening of the first and third harmonics in the drag-force frequency response ($f_{C_x}^* = 1$ and 3) with increasing angle of attack. Odd harmonics indicate a net streamwise force acting on the cylinder during each half cycle. As each major vortex shed by the cylinder results in an impulsive drag force, this implies that the difference in the strength of the shed vorticity between the two half-cycles increases with the angle of attack. Interestingly, we note that a positive correlation between $C_{x rms}$ and α exists for $U^* \leqslant 5$, which is also in line with the trend of the total transverse lift coefficient increasing with the angle of attack over an identical reduced velocity range.

2.2. Wake modes

To further characterise the FIV response when an angle of attack is introduced, the wake structure of the elliptical cylinder in different regimes is examined using particle image velocimetry (PIV) measurements. However, due to the mass ratio of this study being three times that of the study by Lo et al. (2023), the effect that the increased mass has on the FIV of the $\varepsilon = 5$ elliptical cylinder must first be ascertained. Whilst the wake structure of Regime II in this study is almost identical to that reported by Lo et al. (2023), slight differences can be observed for Regime I. As shown in Fig. 7, the increase in the mass ratio of this study as compared to Lo et al. (2023) introduces additional vorticity in the near-wake region, between the pair of large counter-rotating vortices (i.e. the 2S wake mode as defined by Williamson and Roshko (1988)) shed every body oscillation cycle that is the dominant feature of the wake. This additional region of vorticity forms a secondary 2S wake structure (sub–2S) owing to its smaller size and much weaker strength when compared to the major 2S pattern. It is also interesting to note that, unlike the major 2S pattern, the positioning of vorticity in the sub-2S structure is inverted such that the corresponding counter-clockwise vortices are situated above the clockwise vortices (i.e. in the y direction).

After ascertaining the changes in the wake structure due to the increased mass ratio, the wake structures corresponding to each regime identified in the present study are to be characterised. The primary focus of this wake visualisation campaign is on the $\alpha = 2.5°$ response, owing to the presence of all the synchronisation regimes that are identified in this study. Figs. 8–12 show the phase-averaged vorticity contours at $U^* \in \{3.2, 5.0, 5.8, 6.2, 7.0\}$, respectively, to illustrate the wake patterns for each synchronisation regime. Not shown are the wake-body interactions in the desynchronisation region since no discernible regular wake structures are observed.
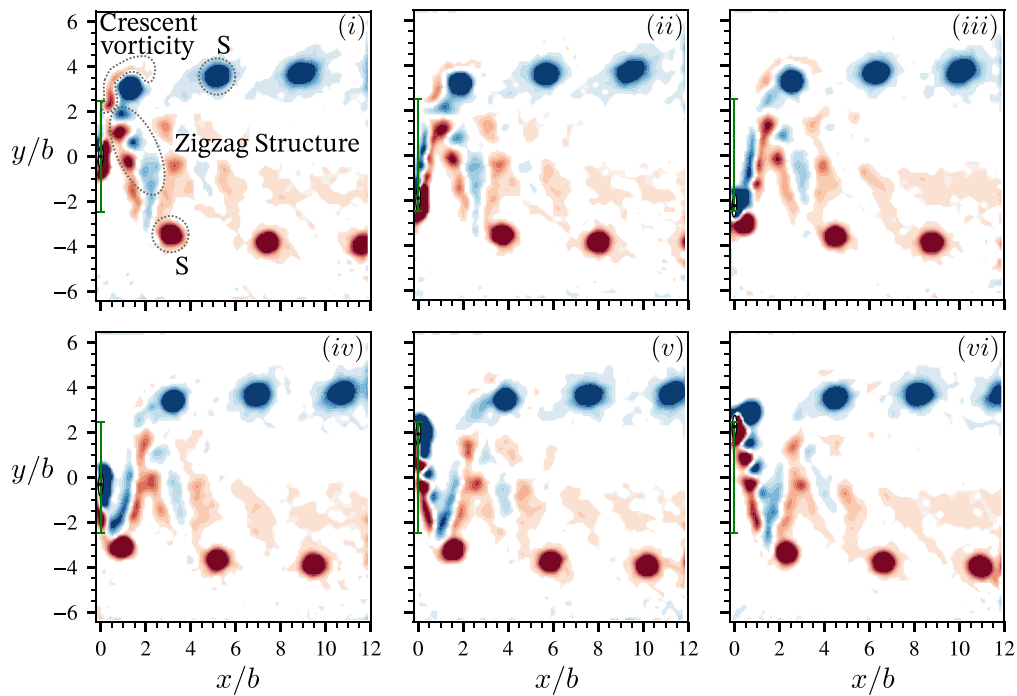
Fig. 9. Evolution of phase-averaged vorticity contours for $\alpha = 2.5°$ at $U^* = 5.0$ (Regime II). More details can be found in the caption of Fig. 7. Whilst the dominant flow structure, like Regime I, is the 2S wake mode, the sub-2S wake component is replaced by a zigzag pattern of vorticity. In addition, a crescent-shaped structure is observed around and is advected along with the clockwise vortex of the major 2S mode.
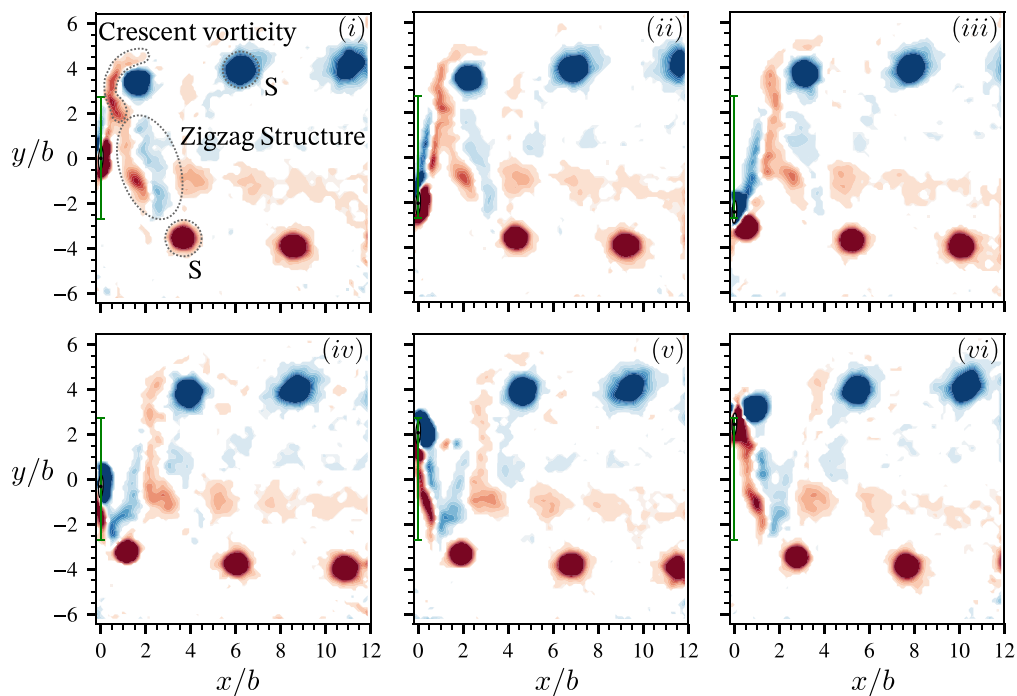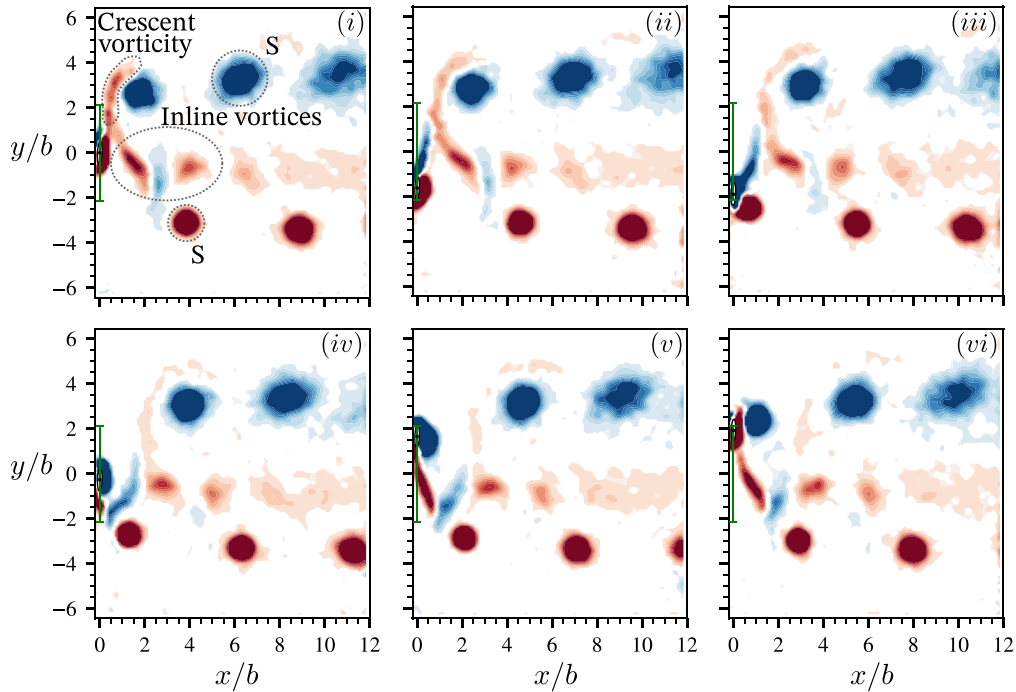

Fig. 10. Evolution of phase-averaged vorticity contours for $\alpha = 2.5°$ at $U^* = 5.8$ (A1). More details can be found in the caption of Fig. 8. With the exception of the continued attachment of the crescent-shaped region to zigzag wake mode and the anti-clockwise vortical component of the zigzag pattern becoming more concentrated towards the negative y^* direction, the flow structure is almost identical to that found in Regime II.

Fig. 11. Evolution of phase-averaged vorticity contours for $\alpha = 2.5°$ at $U^* = 6.2$ (Regime A2). More details can be found in the caption of Fig. 7. Though still predominantly a 2S wake mode, the zigzag pattern of Regimes II and A1 is replaced by a pair of secondary counter-rotating vortices that are shed in an in-line formation (i.e. the vortices have almost the same cross-flow y position).

The major wake structure encountered in all the synchronisation regimes is the 2S pattern, which is primarily responsible for the dominant frequency component of both the body vibration and vortex shedding process (see the PSD contours of f_y^*, as well as $f_{C_y}^*$ and $f_{C_Y}^*$, being close to f_{nw}). Whilst the presence of the second and third harmonic components observed in the fluid forcing can be partially attributed to the unequal strength of the clockwise and anti-clockwise vortices due to the non-zero angles of attack, the additional vortical structures identified for each synchronisation regime also contribute to the harmonics in the fluid forcing.

As mentioned above, the additional vortical structure in Regime I arises due to the presence of the sub–2S wake component that resides between the clockwise and anticlockwise vortex trajectories of the major 2S wake pattern. When comparing Fig. 8 with Fig. 7, the sub–2S pattern appears more well-defined, suggesting that the strength of this secondary wake structure is dependent on the asymmetry of the system.

For Regime II, the observed wake structure bears a marked resemblance to that reported by Lo et al. (2023) for the same regime. Their hydrogen-bubble visualisations show that the zigzag structure between the major 2S vortex street could form a secondary vortex street (SVS). Due to the similarity between the SVS and the vortex signature observed for a NACA0012 airfoil under non-zero angles of attack (Kurtulus, 2016; Gupta et al., 2023), Lo et al. (2023) further argued that the SVS implies the occurrence of flow attachment over the lateral sides of the elliptical cylinder as the body translates across the flow. Interestingly, as a result of the slight angle of attack in Fig. 9(*i*), the anti-clockwise part of the zigzag structure extends and wraps around the most upstream clockwise vortex in the main 2S wake pattern. In Fig. 9(*i-ii*), the clockwise vorticity cuts through the anti-clockwise component of the zigzag and creates a new crescent-shaped structure of anti-clockwise vorticity that is advected downstream along with the clockwise vortex of the 2S pattern. This asymmetric vorticity distribution about the centreline (i.e. $y^* = 0$) likely explains the strengthening of the second harmonic contribution to the fluid forcing in Regime II as α is increased.

Furthermore, the strength of the crescent-shaped wake structure becomes even more pronounced for the first asymmetric regime (A1) as shown in Fig. 10. Unlike Regime II where the crescent-shaped structure is clearly separated from the rest of the zigzag structure, these structures remain attached until diffusion and cross-annihilation intervene further downstream. Moreover, the anti-clockwise vortical component of the zigzag structure becomes more concentrated towards the negative y^* direction. This concentration of secondary vorticity (i.e. outside the 2S wake mode) towards the bottom of the PIV frame further intensifies in the second asymmetric regime (A2) and results in the complete disappearance of the zigzag structure from the wake as shown in Fig. 11. Unlike Regime A1, where the secondary flow structure appears as a sub–2S wake pattern, the secondary vortical signatures are now shed in an in-line arrangement with the location approximately at $y^* = -1$. Again, this offset position and the continued presence of the crescent-shaped structure are likely contributors to the second harmonic being the dominant fluid forcing frequency component in this wake-body synchronisation regime.

Finally, as shown in Fig. 12, the wake structure corresponding to Regime III is characterised by the complete absence of the zigzag structure and secondary vortex streets (both sub–2S and inline arrangements), in direct contrast with the previously discussed
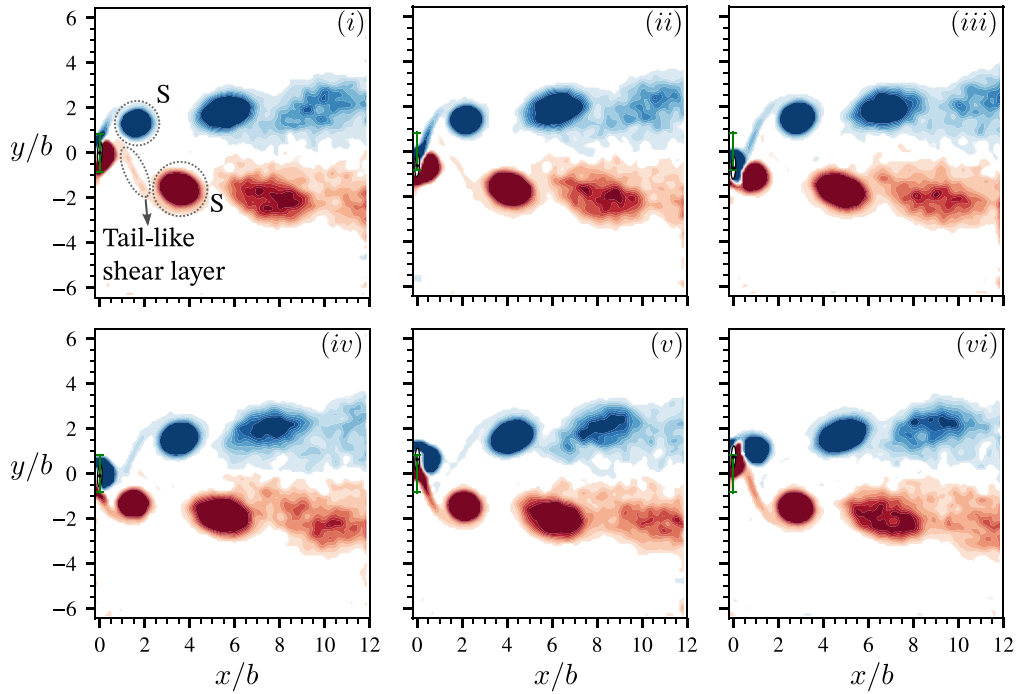
Fig. 12. Evolution of phase-averaged vorticity contours for $\alpha = 2.5°$ at $U^* = 7.0$ (Regime III). More details can be found in the caption of Fig. 7. The predominant flow structure is a 2S wake pattern, with a quickly diffusing tail-like shear layer that connects the shed vortex to the elliptical cylinder.

regimes (i.e. Regime I, II, A1, and A2). Instead, and similarly reported by Lo et al. (2023), the ancillary wake structure consists of a thin shear layer that forms a tail that connects the major vortices to the elliptical cylinder. This feature, which contributes to the very weak second and third harmonic components in $f^*_{C_y}$ and $f^*_{C_v}$, is short-lived and is quickly dissipated by the free-stream flow. Additionally, as signified by the jump in the phase difference from $\phi_y \approx 10°$ (corresponding to Regimes I and II) to $\phi_y \approx 180$, a switch in the timing of the vortex shedding of the main 2S mode is observed. Furthermore, Regime III is the only wake-body synchronisation regime that is almost identical to the wake structure reported by Lo et al. (2023) for the same regime, even when an angle of attack is introduced. This marked resemblance, along with the strong overlap of the amplitude response curves in Regime III (see Fig. 3($a.i$)), indicates that this wake-body synchronisation regime is insensitive to small angles of attack.

3. Conclusions

The present experimental results for an $\varepsilon = 5$ elliptical cylinder have demonstrated that the large amplitudes observed in Regime II decrease with the angle of attack, resulting in its substantial reduction for $\alpha \gtrsim 2°$. This striking reduction in the oscillation amplitude at small α arises due to the movement-induced instability that drives the galloping-like component of the FIV dynamics being strongly affected by any breaking of the inherent symmetry in the system. Furthermore, in addition to I, II, and III wake-body synchronisation regimes that exist for the baseline case ($\alpha = 0°$), two "asymmetric" regimes were observed when an angle of attack was introduced. These asymmetric regimes are broadly classified by the second harmonic in the transverse fluid force frequency response ($f^*_{C_y} \simeq 2$) being one of the dominant frequency components. Furthermore, flow visualisation using PIV has shown that whilst the 2S wake mode remains the primary flow structure in the wake, the increase in the angle of attack results in asymmetric wake patterns. Interestingly, the extent of this asymmetry in the wake varies across the five different wake-body synchronisation regimes, with new wake patterns observed, which were absent for the symmetric case.

These new wake patterns primarily occurred in the asymmetric regimes (i.e. A1 and A2), with two of particular interest. The first is the crescent-shaped structure of anti-clockwise vorticity located around the most upstream clockwise vortex of the main 2S mode, and the second is the inline secondary vortices with an asymmetric centreline (i.e. location of the line is not $y^* = 0$). Although both asymmetric regimes are characterised by the second harmonic being the dominant frequency component in the fluid forcing (as opposed to the first harmonic for Regime I, II and III), the first harmonic component is significantly weaker for A1 than A2, with both harmonics of comparable strength in the latter regime. Furthermore, the effect of small increases in α has a minimal impact on the overall wake structure corresponding to the regimes present in the symmetric case (i.e. I, II, and III), with the only noticeable difference being the appearance of a crescent-shaped region of vorticity enveloping the most upstream clockwise vortex in the main 2S wake pattern.

As such, the above findings indicate that the contribution of movement-induced galloping to the FIV dynamics of the thin elliptical cylinder is highly susceptible to axial asymmetry. With efficient energy conversion from body vibrations predicated upon maximising the vibration amplitude, the flow incidence is an essential parameter that must be accounted for when designing potential FIV-based energy harvesting devices that utilise this particular geometry.

CRediT authorship contribution statement

Jonathan C.C. Lo: Conceptualization, Data curation, Formal analysis, Investigation, Methodology, Software, Writing – original draft. **Mark C. Thompson:** Conceptualization, Project administration, Resources, Supervision, Writing – review & editing. **Kerry Hourigan:** Conceptualization, Funding acquisition, Supervision, Writing – review & editing. **Jisheng Zhao:** Conceptualization, Funding acquisition, Methodology, Project administration, Resources, Writing – review & editing.

Declaration of competing interest

The authors declare that they have no known competing financial interests or personal relationships that could have appeared to influence the work reported in this paper.

Data availability

Data will be made available on request.

Acknowledgements

References

Bernitsas, M.M., Raghavan, K., Ben-Simon, Y., Garcia, E.M.H., 2008. VIVACE (Vortex Induced Vibration Aquatic Clean Energy): A new concept in generation of clean and renewable energy from fluid flow. J. Offshore Mech. Arct. Eng. 130 (4), 041101.

Blevins, R.D., 1990. Flow-Induced Vibration, second ed. Krieger Publishing Company.

Ding, L., Zhang, L., Bernitsas, M.M., Chang, C.-C., 2016. Numerical simulation and experimental validation for energy harvesting of single-cylinder VIVACE converter with passive turbulence control. Renew. Energy 85, 1246–1259.

Fouras, A., Lo Jacono, D., Hourigan, K., 2008. Target-free stereo PIV: A novel technique with inherent error estimation and improved accuracy. Exp. Fluids 44 (2), 317–329.

Govardhan, R., Williamson, C.H.K., 2000. Modes of vortex formation and frequency response of a freely vibrating cylinder. J. Fluid Mech. 420, 85–130.

Gupta, S., Zhao, J., Sharma, A., Agrawal, A., Hourigan, K., Thompson, M.C., 2023. Two-and three-dimensional wake transitions of a NACA0012 airfoil. J. Fluid Mech. 954, A26.

Khalak, A., Williamson, C.H.K., 1996. Dynamics of a hydroelastic cylinder with very low mass and damping. J. Fluids Struct. 10 (5), 455–472.

Kurtulus, D.F., 2016. On the wake pattern of symmetric airfoils for different incidence angles at Re=1000. Int. J. Micro Air Veh. 8 (2), 109–139.

Leontini, J.S., Griffith, M.D., Lo Jacono, D., Sheridan, J., 2018. The flow-induced vibration of an elliptical cross-section at varying angles of attack. J. Fluids Struct. 78, 356–373.

Lo, J.C.C., Hourigan, K., Thompson, M.C., Zhao, J., 2023. The effect of structural damping on flow-induced vibration of a thin elliptical cylinder. J. Fluid Mech. 974, A5.

Lv, Y., Sun, L., Bernitsas, M.M., Sun, H., 2021. A comprehensive review of nonlinear oscillators in hydrokinetic energy harnessing using flow-induced vibrations. Renew. Sustain. Energy Rev. 150, 111388.

Massai, T., Zhao, J., Lo Jacono, D., Bartoli, G., Sheridan, J., 2018. The effect of angle of attack on flow-induced vibration of low-side-ratio rectangular cylinders. J. Fluids Struct. 82, 375–393.

McQueen, T., Zhao, J., Sheridan, J., Thompson, M.C., 2021. Vibration reduction of a sphere through shear-layer control. J. Fluids Struct. 105, 103325.

Morse, T.L., Williamson, C.H.K., 2009. Prediction of vortex-induced vibration response by employing controlled motion. J. Fluid Mech. 634, 5.

Naudascher, E., Rockwell, D., 2017. Flow-Induced Vibrations: An Engineering Guide. Routledge.

Navrose, Yogeswaran, V., Sen, S., Mittal, S., 2014. Free vibrations of an elliptic cylinder at low Reynolds numbers. J. Fluids Struct. 51, 55–67. http://dx.doi.org/10.1016/j.jfluidstructs.2014.07.012.

Nemes, A., Zhao, J., Lo Jacono, D., Sheridan, J., 2012. The interaction between flow-induced vibration mechanisms of a square cylinder with varying angles of attack. J. Fluid Mech. 710, 102–130.

Païdoussis, M.P., Price, S.J., De Langre, E., 2010. Fluid-Structure Interactions: Cross-Flow-Induced Instabilities. Cambridge University Press.

Sherry, M., Lo Jacono, D., Sheridan, J., 2010. An experimental investigation of the recirculation zone formed downstream of a forward facing step. J. Wind Eng. Ind. Aerodyn. 98 (12), 888–894.

Soti, A.K., Zhao, J., Thompson, M.C., Sheridan, J., Bhardwaj, R., 2018. Damping effects on vortex-induced vibration of a circular cylinder and implications for power extraction. J. Fluids Struct. 81, 289–308.

Wang, Z., Du, L., Zhao, J., Sun, X., 2017. Structural response and energy extraction of a fully passive flapping foil. J. Fluids Struct. 72, 96–113.

Williamson, C.H.K., Roshko, A., 1988. Vortex formation in the wake of an oscillating cylinder. J. Fluids Struct. 2 (4), 355–381.

Wong, K.W.L., Zhao, J., Jacono, D.L., Thompson, M.C., Sheridan, J., 2017. Experimental investigation of flow-induced vibration of a rotating circular cylinder. J. Fluid Mech. 829, 486–511.

Zhao, J., Hourigan, K., Thompson, M., 2018a. Flow-induced vibration of D-section cylinders: An afterbody is not essential for vortex-induced vibration. J. Fluid Mech. 851, 317–343.

Zhao, J., Hourigan, K., Thompson, M., 2019. Dynamic response of elliptical cylinders undergoing transverse flow-induced vibration. J. Fluids Struct. 89, 123–131.

Zhao, J., Leontini, J.S., Lo Jacono, D., Sheridan, J., 2014a. Chaotic vortex induced vibrations. Phys. Fluids 26 (12), 121702.

Zhao, J., Leontini, J.S., Lo Jacono, D., Sheridan, J., 2014b. Fluid–structure interaction of a square cylinder at different angles of attack. J. Fluid Mech. 747, 688–721.

Zhao, J., Leontini, J.S., Lo Jacono, D., Sheridan, J., 2014c. Fluid–structure interaction of a square cylinder at different angles of attack. J. Fluid Mech. 747, 688–721.

Zhao, J., Lo Jacono, D., Sheridan, J., Hourigan, K., Thompson, M.C., 2018b. Experimental investigation of in-line flow-induced vibration of a rotating circular cylinder. J. Fluid Mech. 847, 664–699.

Zhao, J., Thompson, M.C., Hourigan, K., 2022. Decomposition of fluid forcing and phase synchronisation for in-line vortex-induced vibration of a circular cylinder. J. Fluid Mech. 941, R4.